CONDENSED MATTER PHYSICS

Probing the low-temperature limit of the quantum anomalous Hall effect

Lei Pan[1]*, Xiaoyang Liu[2]*, Qing Lin He[1,3]*, Alexander Stern[4,5], Gen Yin[1], Xiaoyu Che[1], Qiming Shao[1,6], Peng Zhang[1], Peng Deng[1], Chao-Yao Yang[1], Brian Casas[4], Eun Sang Choi[7], Jing Xia[4], Xufeng Kou[2], Kang L. Wang[1,8,9†]

Quantum anomalous Hall effect has been observed in magnetically doped topological insulators. However, full quantization, up until now, is limited within the sub–1 K temperature regime, although the material's magnetic ordering temperature can go beyond 100 K. Here, we study the temperature limiting factors of the effect in Cr-doped $(BiSb)_2Te_3$ systems using both transport and magneto-optical methods. By deliberate control of the thin-film thickness and doping profile, we revealed that the low occurring temperature of quantum anomalous Hall effect in current material system is a combined result of weak ferromagnetism and trivial band involvement. Our findings may provide important insights into the search for high-temperature quantum anomalous Hall insulator and other topologically related phenomena.

INTRODUCTION

The quantum Hall effect (QHE), which was first observed in two-dimensional (2D) electron gas systems, demonstrates the first example of a quantum state that is topologically distinct from other condensed matters. Under a strong external magnetic field, the QHE edge states emerging at the sample boundary exhibit the chiral dissipationless transport nature with a vanishing longitudinal resistance and a quantized Hall conductance of ve^2/h (where v is the Landau level index, e is the electron charge, and h is the Planck constant). Such a transport signature, if the requirement of high magnetic field can be removed, would unveil tremendous opportunities in low-power electronic applications (*1*). This inspires an upsurge in searching for a zero-field version of QHE for more than three decades. One such version is known as the quantum anomalous Hall effect (QAHE) (*2*–*6*). A topologically nontrivial electronic structure with time-reversal symmetry broken by magnetic moment instead of an external magnetic field is one of the most promising systems to host the QAHE. Recently, the QAHE was demonstrated experimentally in magnetically doped topological insulators (MTIs), e.g., Cr/V:$(Bi,Sb)_2Te_3$, where the utilization of both the intrinsic strong spin-orbit coupling (SOC) and the incorporated long-range out-of-plane ferromagnetic (FM) order give rise to the chiral edge state with a nonzero Chern number (*7*, *8*). However, to date, the observation of the QAHE state is yet limited to extremely low temperatures (below 1 K), although some host MTIs have a Curie temperature above 170 K (*9*, *10*). As a result, the underlying physics of this temperature limit has remained to be an open question so far (*9*, *11*–*16*).

To address this issue, earlier attempts have been focusing on understanding the FM origins and exploring the possible band structure modifications caused by the magnetic dopants. From the FM ordering aspect, the presence of superparamagnetic domains and their dynamics are believed to hinder the formation of a strong uniform FM order in the MTIs (*13*, *17*), while from the band structure point of view, the presence of both the magnetic impurity bands and the bulk valence band near the Fermi level could also introduce additional dissipative conduction channels and hence deteriorate the transport signature of the QAHE (*18*–*20*). These findings all suggest sophisticated coupling mechanisms among the SOC, FM ordering, dopant profile, and film structure in realizing the QAHE (*21*). Consequently, a QAHE platform in which all these key parameters can be manipulated individually is of great demand before pushing the limit of the QAHE toward room temperature. In this work, a set of MTI thin films are prepared with a wide tuning range of thickness and doping profile, with which the limiting factors to the onset of the QAHE can be systematically investigated. An intricate interplay between the FM order and the band structure is demonstrated by investigating the quantum transport signature, activation behavior, magneto-optic response, and the QAHE phase transition diagram. The activation behavior of the QAHE is found to be closely related to the gap between the Fermi level and its nearest bulk/impurity band edge. The tracing of such a gap in samples with various thicknesses and the external magnetic field points to different origins of temperature limiting factors. This QAHE activation gap can serve as a benchmark of the QAHE and provide a guide for searching high-temperature QAHE material and heterostructures toward robust and functional QAHE states.

RESULTS AND DISCUSSION

Global phase diagram of QAHE in various thicknesses

Using an optimized MTI thin-film growth procedure established from our previous work (*11*, *22*), a set of high-quality $(Cr_{0.12}Bi_{0.26}Sb_{0.62})_2Te_3$ samples with film thickness ranging from 6 to 10 quintuple layers (QLs) were epitaxially grown with the Fermi level positioned inside

[1]Department of Electrical and Computer Engineering, University of California, Los Angeles, Los Angeles, CA 90095, USA. [2]School of Information Science and Technology, ShanghaiTech University, Shanghai 200031, China. [3]International Center for Quantum Materials, School of Physics, Peking University, Beijing 100871, China. [4]Department of Physics and Astronomy, University of California, Irvine, Irvine, CA 92697, USA. [5]Max Planck Institute for Chemical Physics of Solids, Nöthnitzer Straße 40, 01187 Dresden, Germany. [6]Department of Electronic and Computer Engineering, The Hong Kong University of Science and Technology, Clear Water Bay, Kowloon, Hong Kong SAR, China. [7]National High Magnetic Field Laboratory, Florida State University, Tallahassee, FL 32310-3706, USA. [8]Department of Materials Science and Engineering, University of California, Los Angeles, Los Angeles, CA 90095, USA. [9]Department of Physics, University of California, Los Angeles, Los Angeles, CA 90095, USA.
*These authors contributed equally to this work.
†Corresponding author. Email: wang@ee.ucla.edu

the surface magnetic exchange gap without additional gate tuning. Figure 1 summarizes the magneto-transport results of three uniformly doped $(Cr_{0.12}Bi_{0.26}Sb_{0.62})_2Te_3$ samples with film thicknesses of 6, 8, and 10 QLs, respectively. At 20 mK, all three samples exhibit a fully quantized Hall resistance ($\rho_{yx} = \pm h/e^2$) at zero magnetic field, highlighting the realization of QAHE. The resistance fluctuation close to zero magnetic field is a result of unstable temperature, with more details explained in the Supplementary Materials.

Notably, the detailed quantum conductance and topological phase transition exhibit distinct features among the three samples. Specifically, at the extreme 2D limit, i.e., the six-QL MTI sample, the top and bottom surfaces will strongly hybridize, resulting in the topological quantum phase transition between the $\pm h/e^2$ states (i.e., with Chern number $C = \pm 1$, respectively) (*23*). As discussed in our previous work (*22*, *23*), the surface hybridization gap due to the quantum confinement of the six-QL MTI sample would compete with the magnetic exchange gap, whose magnitude is determined by the FM order. Accordingly, when the FM moment is minimized during the magnetization reversal, the dominant hybridization gap would give rise to a topologically trivial insulating state with $C = 0$. Experimentally, this emergent topological quantum transition is shown in Fig. 1 (D and G), where σ_{xx} of the six-QL sample goes through two peaks separating the $C = \pm 1$ and 0 states (all of which have zero σ_{xx} value), and σ_{xy} develops zero-conductance Hall plateaus at $C = 0$ between $\pm h/e^2$ states during each sweep (the orange/blue colored traces represent the different field sweep directions). Here, it is noted that the $C = 0$ insulating

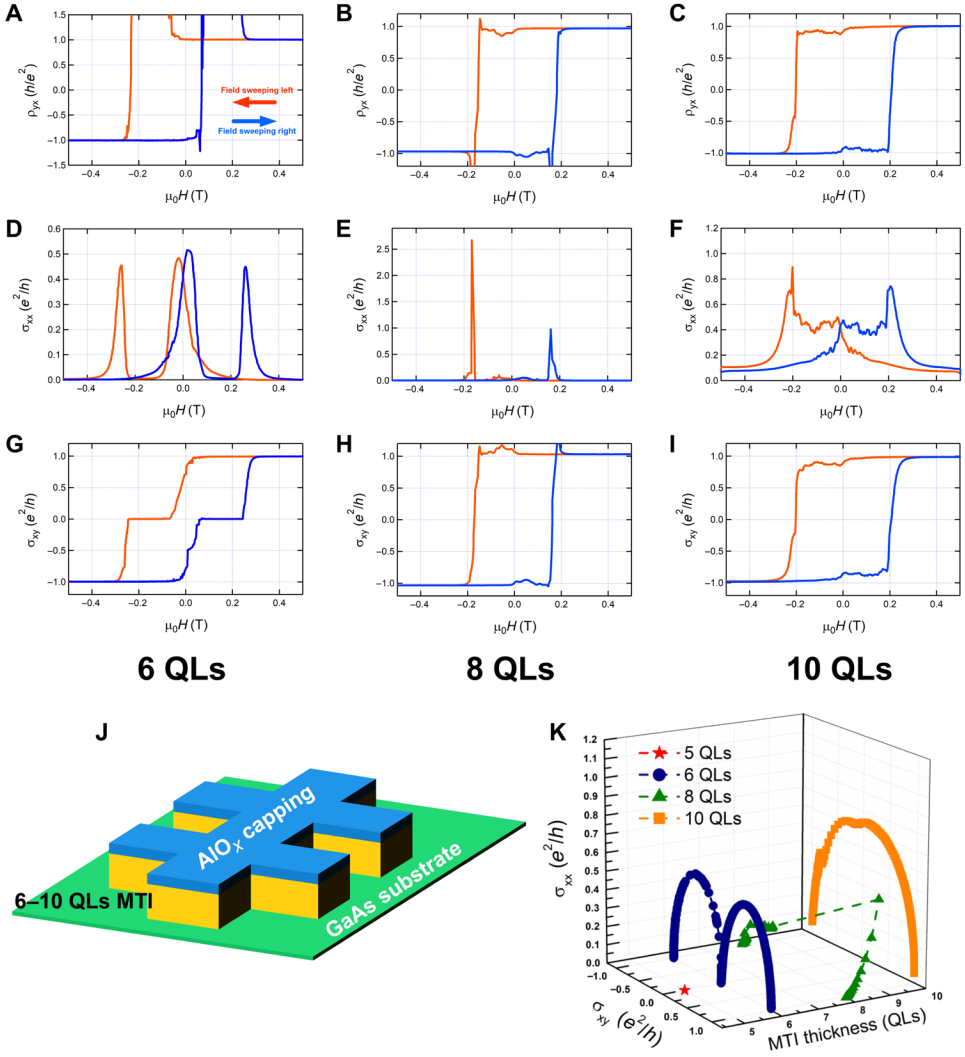

Fig. 1. QAHE realized in different thicknesses of MTIs. Curves in red indicate the magnetic field sweeping from the positive to the negative direction, and blue curves indicate the reverse trace. (**A** to **C**) Hall resistivity versus external magnetic field for samples with thicknesses of 6, 8, and 10 QLs, respectively. All samples show Hall resistivity quantized at $\pm h/e^2$ at zero magnetic field. For (A), the transition part of the data is not shown due to the sample's extremely insulating behavior. (**D** to **F**) Longitudinal conductivity for the same set of MTIs. At zero magnetic field, 8 QLs show vanishing longitudinal conductivity and 10 QLs still have a finite longitudinal conductivity, yet the 6-QL MTI shows a split double-peak behavior around the coercive field and nonzero longitudinal conductivity. (**G** to **I**) Hall conductivity for the same set of MTIs. At zero magnetic field, 8- and 10-QL MTIs show quantized σ_{xy} at e^2/h. The six-QL MTI (G) shows zero-Hall plateaus at coercive field and deviation from perfect quantized $\pm e^2/h$ when the external field is approaching zero. (**J**) Schematic drawing of the MTI samples. (**K**) Global phase diagram of QAHE for MTIs' thicknesses ranging from 5 to 10 QLs. For five-QL MTI, the hybridization gap dominates the system and drives it into a trivial insulator. For six-QL MTI, the competition between hybridization gap and exchange gap during transition forms a unique double-semicircle transition curve. For 8- and 10-QL samples, the phase transition only happens between the $C = \pm 1$ states.

states exhibit a noisy and high resistance behavior (shown in fig. S1); this can be explained by percolation theory, where the sample entered a random domain state during the switching. The resistance as high as 10 megohms is also, by far, the most insulating state reported in the QAHE systems (*24*, *25*). Furthermore, this insulating state (σ_{xy}, σ_{xx}) = (0, 0) is found to be present across a wide magnetic field range (i.e., ~0.2 T) which not only manifests the unique metal-to-insulator switching of the QAHE state in the 2D limit (*22*) but also offers the opportunity for searching exotic critical quantum phases, for instance, the chiral Majorana edge modes in the QAH/superconductor hybrid system between $C = \pm1$ and $C = 0$ states (*26*, *27*). On the contrary, in thicker MTIs where the hybridization gap becomes negligible, the system is always topologically nontrivial with either Chern number $C = \pm1$. Such a scenario is demonstrated in both the 8- and 10-QL samples, where a sharp transition between the $+h/e^2$ and the $-h/e^2$ edge states takes over in the QAHE hysteresis loop without the presence of any intermediate insulating states, as shown in Fig. 1 (E, F, H, and I).

By achieving the QAH states across a thickness range, we can complete a thickness-dependent QAH phase diagram. As highlighted in Fig. 1K, the (σ_{xy}, σ_{xx}) plot of the six-QL MTI sample follows a double semicircular transition that continuously connects the ($\pm e^2/h$, 0) and (0, 0) states, while the 8- and 10-QL samples only exhibit two stable states at ($\pm e^2/h$, 0). Under the fixed magnetic sweeping speed (0.1 T/min), the eight-QL film shows a single-domain behavior where the transition between the two quantized $C = \pm1$ states is fast, with only a few discrete (σ_{xy}, σ_{xx}) points located along the meta-stable transition route, while the (σ_{xy}, σ_{xx}) plot of the 10-QL sample displays a more continuous feature and the transition loop is found to be slightly deviated from the perfect semicircle contour, which may suggest the presence of additional dissipative conduction path (given that the 10-QL film may possibly have the largest bulk contribution). We notice that when the quantum confinement dominates in the ultrathin MTI film (i.e., five QLs), the hybridization gap [~50 meV according to (*28*, *29*)] will drive the host QAHE system into a topologically trivial insulating state regardless of the external magnetic field (*30*–*32*). Under such circumstances, the five-QL phase diagram reduces to a single point, where σ_{xy} and σ_{xx} both are equal to zero corresponding to the fact that the Fermi level rests inside the trivial surface and bulk gap. In short, the thickness-dependent QAHE results, along with the corresponding QAH phase diagram shown in Fig. 1K, signify the importance of film thickness (or equivalently, the magnetic exchange gap and hybridization gap), thus implying the possibility to enhance the QAH temperature and manipulate QAH states via structural engineering, for which we will discuss in the "Toward high-temperature and functional QAHE" section.

QAH activation gap

In both integer and fractional QHE, the activation energy scale, which is usually extracted from the temperature-dependent σ_{xx} plot, has been widely used to determine the robustness of such quantum state against thermal fluctuation (*33*–*35*). Sharing the same topological nature (*36*), the QAH activation gap (Δ) also carries similar information as its QHE counterpart; hence, it can be investigated by using the same approach. Application wise, this activation gap size, which serves as a benchmark parameter, dictates the viable temperature range to use the dissipationless nature of QAH states. Inspired by the unique thickness-dependent QAH transport behaviors obtained in Fig. 1, we further traced the QAH activation gap in these MTI thin films with different magnetic field responses to better understand the underlying mechanisms, as well as to probe the possible temperature limiting factors. In particular, we attempted to use a single–activation gap Arrhenius equation $\sigma_{xx} = \sigma_0 \cdot \exp\left(-\frac{\Delta}{k_B T}\right)$ to fit the data, yet only succeeded in the high field regime in the six-QL sample, as shown in Fig. 2A. Alternatively, when the external field was smaller than 0.15 T, an additional dissipative conductivity term σ_1 that does not follow the Arrhenius equation had to be included to fit the data such that

$$\sigma_{xx} = \sum_{i=0,1} \sigma_i \cdot \exp\left(-\frac{\Delta_i}{k_B T}\right), \Delta_1 = 0$$

In contrast, the QHE activation behaviors can usually be described by one or few activation energies, which follow Arrhenius equation in either graphene, oxide material, or 2D electron gas systems (*34*, *37*–*39*). Meanwhile, both Δ_0 and σ_1 have a strong field dependence, where the increase of the applied magnetic field results in a larger activation gap and a smaller dissipative component, as depicted in Fig. 2 (D and E). Therefore, we may conclude that to drive the system into a near-perfect QAH state with minimized σ_1, an additional external field (>0.15 T) is required to suppress the dissipative channel caused by the weak ferromagnetism and existence of superparamagnetism in the six-QL sample, as we will elaborate in the next section.

On the other hand, when the thin-film thickness is thicker than six QLs, the activation feature markedly changes. As compared with the 6-QL sample, the activated conduction behaviors of both the 8- and 10-QL samples always include both the dissipative conductivity σ_1 across the entire magnetic field range (0 to 5 T), as shown in Fig. 2D. Unlike the six-QL case, the magnitude of σ_1 in thicker MTI samples is found to gradually increase under larger magnetic field, hence implying a different origin of the dissipative channel rather than the unstable ferromagnetism, as illustrated in Fig. 2D. This phenomenon is commonly observed in metallic systems, where the positive magnetoresistance background is related to the Fermi level crossing the trivial band edges. Besides, it is noted that our results agree well with the recent angle-resolved photoemission spectroscopy (ARPES) study (*18*) focusing on the band structure near the Dirac point of the MTI, which showed the overlapping of the nontrivial surface band with the trivial bulk valence band.

Meanwhile, as summarized in Fig. 2E, the QAH activation gaps Δ_0 in the cases of 8- and 10-QL MTIs are both negatively related to the external magnetic field, which are opposite to the 6-QL scenario. This field-dependent feature highlights the pronounced splitting of the bulk valence band under high magnetic field in the thicker MTI samples (*40*). In general, magnetic dopants can induce an energy splitting between up and down spins, which has been well studied in diluted magnetic semiconductors (*40*, *41*). This splitting comes from the combined effect of the on-sight exchange energy and the Zeeman energy given by the applied field. Here, the MTI system, without considering its topological property, also falls in the category similar to the diluted magnetic semiconductor system (*42*). This band splitting can affect MTI's transport properties if they are included in the thermal window. Here, we summarize and propose a possible band structure picture as shown in Fig. 2F. In the case of six QLs, the bulk-band splitting is pushed away from the surface bands due to the vertical quantum confinement and thus does not strongly affect the transport. However, when thicker than six QLs, the band edges are closer to the Fermi level, and the activation gap Δ_0 may be strongly

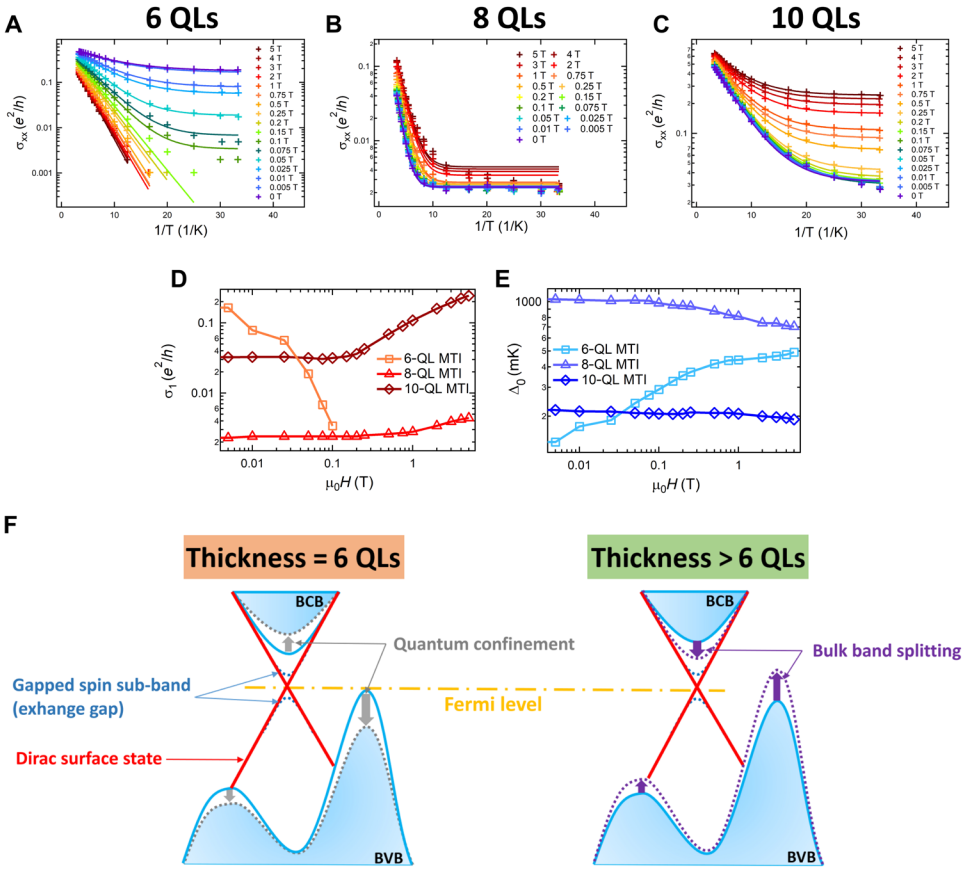

Fig. 2. Thickness-dependent transport behavior of QAHE. (**A** to **C**) σ_{xx} as a function of inverse temperature for 6- 8-, and 10-QL MTIs with modified Arrhenius fit (details in text) under different external magnetic field. (**D** and **E**) Magnetic field dependence of parallel dissipative conductivity (σ_1) and QAH activation energy (Δ_0) of the 6-, 8-, and 10-QL MTIs extracted from (A) to (C) using modified Arrhenius fit. (**F**) Schematic drawing of band structure around Dirac point for thickness equal (left) and larger to six QLs (right). The shifted bulk band edge and its relative position with Fermi level explain the different magnetic field effect on activation energy for MTIs with different thicknesses.

modulated. An increase in the applied field can enlarge the spin splitting, and therefore, Δ_0 decreases. Furthermore, we need to point out that the 8-QL sample shows almost five times larger activation gap and one order of magnitude smaller dissipative term than the 10-QL sample. In addition, thicker MTI samples have another trivial longitudinal resistance component, which is the side surface conduction that has been reported before (*11*). However, this effect has no magnetic field dependence and is not included in our band structure discussion. To sum up, the marked transport result difference again manifests the critical thickness limiting factor in the $(Bi,Sb)_2Te_3$-based QAH system, where the inevitable increased bulk contribution finally prevents the detection of QAHE in even thicker MTI samples.

Magneto-optic Kerr effect

The above transport experiments of the six-QL MTI sample revealed the importance of MTI's ferromagnetism in reaching full quantization. Unlike the 8- and 10-QL MTI samples, it is noted that the conductance σ_{xx} and σ_{xy} of the 6-QL MTI deviate from the quantized value before the external field approaches zero, as shown in Fig. 1 (D and G). Therefore, the need of an additional small external field to realize full quantization may imply the existence of soft magnetic order in the six-QL MTI sample. To directly address this magnetic order, we further performed magneto-optic Kerr effect (MOKE) measurements on one of our six-QL MTI samples. The magneto-optical setup is constructed with a loop-less fiber-optic Sagnac interferometer for better sensitivity, which can accurately measure time-reversal symmetry breaking event down to 10 nano-radians (*43*). Figure 3 (A and B) summarizes both the temperature-dependent Kerr rotation angle and the anomalous Hall resistance R_{yx} results, which are taken simultaneously (see Materials and Methods). It is observed that the magnetic hysteresis behavior revealed by both results is highly consistent across a wide temperature range (70 mK to 28 K) in terms of the coercive field size. Yet, we need to emphasize the major difference between the two sets of data: When the system temperature decreases, the up-ramping of magnetic field quickly drives the Kerr signal to a saturation value around $\sim 10^{-3}$ rad that almost remains the same for up to 4.3 K, as shown in Fig. 3A (i.e., indicating that the magnetization of the MTI sample is fully saturated); in contrast, the R_{yx} value will not reach the quantized h/e^2 value until $T < 700$ mK, as shown in Fig. 3B. This finding may suggest that the robust macroscopic FM order alone does not necessarily guarantee the dissipationless quantum transport in our MTI system.

As mentioned in the previous section, we have identified the presence of a dissipative conductivity σ_1 when the applied magnetic field is smaller than 0.15 T and related this term to the weak ferromagnetism in the six-QL MTI. Using optical technique, here, we are able

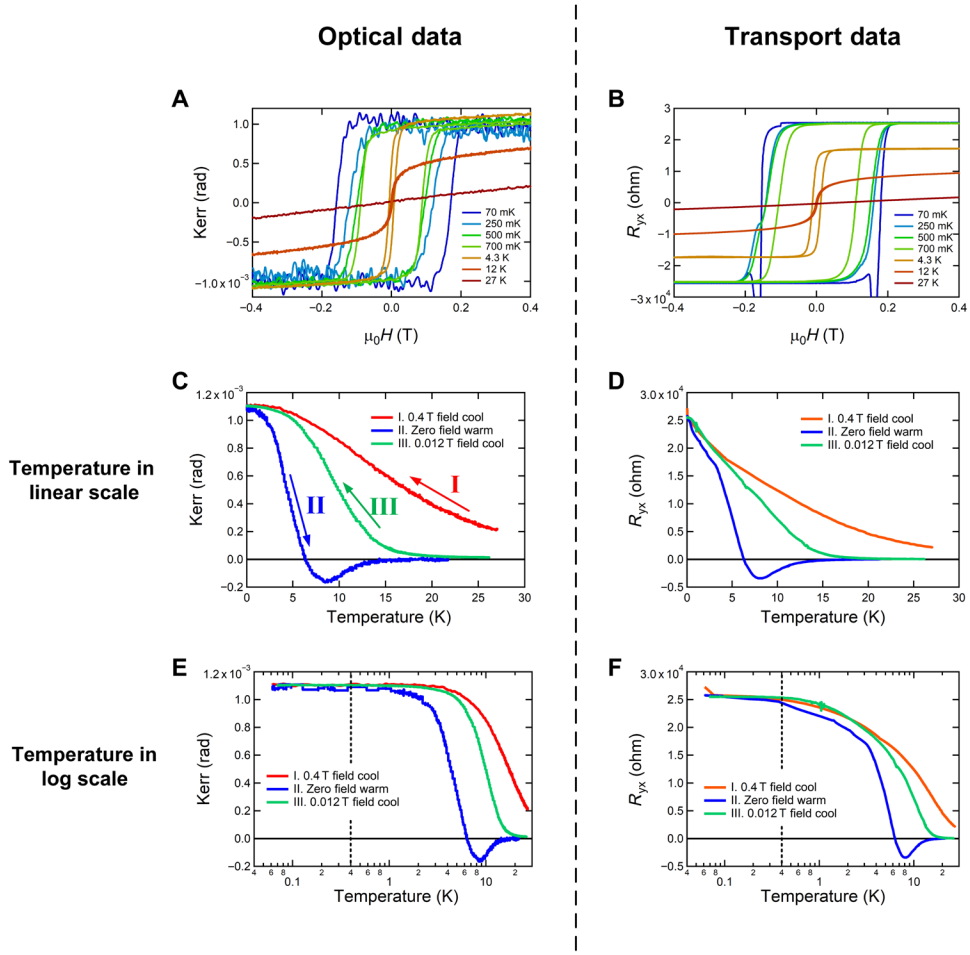

Fig. 3. Concurrent magneto-optic Kerr effect and transport measurements of six-QL MTI. The magneto-optic setup is enhanced by Sagnac interferometer. (**A** and **B**) Hysteresis loops of Kerr rotation angle and Hall resistance at different temperatures. The FM behavior of six-QL MTI disappears at 27 K. (**C** and **D**) Kerr rotation angle and Hall resistance under different field cooling and warming schemes. Under zero field warming, both Kerr rotation angle and Hall resistance undergo a sign flipping during the process, indicating an unstable ferromagnetism inside this six-QL MTI. (**E** and **F**) Replot of (C) and (D) by using log scale for temperature. The expansion of low temperature data reveals the saturation of the Kerr rotation angle, and the Hall resistance occurs at a much lower temperature regime (<400 mK) than the Curie temperature, which indicates another temperature scale that is related to six-QL MTI's ferromagnetism and superparamagnetism observed.

to confirm the existence of superparamagnetism in our sample, as some groups have reported similar findings using different techniques.

The first evidence is in the hysteresis loop scan shown in Fig. 3 (A and B), where coercivity nearly vanishes above 12 K for both optical and transport measurements, although there is still a noticeable magnetic moment. This is often observed in a low dimensional magnetic system (*44*, *45*).

Followed by the measurements tracing both temperature-dependent Kerr signal and R_{yx} signals by using different field cooling/warming schemes as shown in Fig. 3 (C to F), the second evidence is that in the linear-scale plot (Fig. 3, C and D), the temperature-dependent Kerr rotation signal during the field cooling ($\mu_0 H$ = 400 and 12 mT) process does not follow classic Curie-Weiss type of spontaneous magnetization behavior in a typical ferromagnet (detailed information of a typical ferromagnet $SrRuO_3$ is provided in fig. S2) (*46*). The evident discrepancy between the two field-cooling curves (red and green in Fig. 3, C and D) acquired under different magnetic fields suggests that the magnetism of six-QL MTI is not strong enough to yield a robust order without the assistance of external field.

The third evidence is that during the succeeding zero-field warming process (step 2 curve in Fig. 3, C and D, respectively), the curves' deviation from the saturation magnetization starts as early as 400 mK (blue trace in Fig. 3, E and F; T = 400 mK is highlighted with dashed line), which is almost two orders of magnitude lower than MTI's perceived Curie temperature (~20 K). In addition, the zero-field warming curves for Kerr and R_{yx} signal go to near zero when the base temperature reaches above 14 K. It may be attributed to the spin relaxation due to the competition between the magnetic anisotropy energy KV (K is the magnetocrystalline anisotropy constant and V is the nanomagnet volume) versus the thermal fluctuation energy $k_B T$, as the origin of superparamagnetism (*47*). In addition, we observed a rather abnormal sign change of both the Kerr rotation signal and the Hall voltage during the zero-field warming process within the [6 K, 14 K] regime. The reason of this magnetization flipping at elevated temperature is not clear yet, but it has also been observed in some magnetic systems with complicated spin configurations (*48*, *49*). The effect arising from the antiferromagnetically coupled Cr/Sb and Te moment identified using x-ray magnetic circular dichroism technique

(*50*, *51*) might participate in this phenomenon, which requires further investigation.

To conclude this part, we confirmed the existence of superparamagnetism in the six-QL uniform-doped MTI. The magnetic anisotropy energy scale of the superparamagnetism when converted to temperature (T_{KV}) should be much lower than the Curie temperature T_C given that the onset of QAHE happens only at $T < 700$ mK. As a result, superparamagnetic domains may form inside the film (*20*) over a relatively wide temperature range, and the misalignment of such domains may account for the small QAHE activation gap Δ_0 as well as the parallel dissipative conductivity σ_1 in the hybridized 2D MTI system. Therefore, to solve this problem, major effort should focus on improving MTIs with not only more robust but also more uniform FM order.

Toward high-temperature and functional QAHE

So far, we have identified two methods that may help to increase the QAH gap, namely, the uniform single-domain FM texture and the minimized dissipative bulk conduction channel. For the case of thicker MTI films, the realization of QAHE is limited by the intrinsic band structure (i.e., the small thermal window between the Fermi level and the bulk valence band as shown in Fig. 2F). Therefore, to enlarge the thermal window, additional elemental doping [e.g., Sn or S (*52*, *53*)] is required to modify the bulk valence band. However, the involvement of such high vapor pressure elements would inevitably make it more difficult to precisely control the chemical composition of the MTI sample during sample growth (*22*). Alternatively, as we demonstrated in the "QAH activation gap" section, the 2D MTI system turns out to be a better platform for the pursuit of high-temperature QAHE, because the parallel bulk conduction is minimized and the dissipative conductivity σ_1 (due to the multidomain and superparamagnetic texture) can be suppressed with the assistance of the external magnetic field. Accordingly, to further stabilize the magnetic domain and to increase the QAHE exchange gap Δ_0 at zero magnetic field, we introduce structural engineering on the 2D MTI system by modifying the dopant profile in the six-QL MTI candidates.

To experimentally validate the above proposal, we prepared two additional 2D MTI samples with different structures: one is a uniformly doped six QLs $(Cr_{0.16}Bi_{0.25}Sb_{0.59})_2Te_3$ with higher Cr doping of 16% and the other one is a trilayer structure sample, where both the top and bottom surfaces (i.e., with a thickness of one QL) are heavily doped by Cr (~24%), while the bulk four QLs remain as the $(Cr_{0.12}Bi_{0.26}Sb_{0.62})_2Te_3$ composition, as illustrated in Fig. 4A. It is found that the higher uniform Cr-doping MTI showed similar transport behavior as the one with original recipe, as shown in Fig. 4D. In contrast, for the trilayer modulation-doped MTI, the activated conduction plot shown in Fig. 4B is governed by the single-gap picture without the presence of the dissipative σ_1 contribution even at zero magnetic field. More notably, the measured QAH activation gap $\Delta_0 = 80$ μeV is more than four times larger than the uniform MTI counterpart at zero field, and is almost insensitive to external magnetic field, as highlighted in Fig. 4C. Concurrently, the longitudinal and Hall conductance in this trilayer six-QL MTI sample perfectly quantized at $(\sigma_{xx}, \sigma_{xy}) = (0, \pm h/e^2)$ at zero field (shown in fig. S4), hence manifesting the formation of a robust spontaneous FM order. Here, we need to point out that the onset of QAHE in the trilayer sample is still around $T = 1$ K due to the relatively small magnetic exchange gap. [Several studies suggested the inhomogeneity of magnetic dopants could effectively smear out the exchange gap (*54*, *55*).] Nevertheless, the use of the trilayer configuration by structural engineering unveils an effective way to a more robust QAH state and potentially can lead to higher QAH onset temperature.

In addition, it is also noted that while a more robust remnant quantized state in the modulation-doped six-QL MTI films was achieved, the flat zero-Hall plateaus have narrowed down to 0.04 T, as shown in Fig. 4D. As discussed above, the exchange gap by modulation doping effectively modulates the relative strength between Δ_M (exchange gap size) and m_0 (hybridization gap size) especially during the magnetization reversal process, where the filling factor C is related to parameters as (*23*)

$$C = \begin{cases} \frac{\Delta_m}{|\Delta_m|}, \text{for } |\Delta_m| > |m_0| \\ 0, \text{for } |\Delta_m| < |m_0| \end{cases}$$

The size of the zero-Hall plateaus is a key factor to successfully observing the chiral Majorana edge mode. By using different doping profile, we are able to control the width effectively. Consequently, this doping strategy can serve as an additional degree of freedom to control the chiral Majorana edge mode based on the MTI/superconductor heterostructure (*27*).

CONCLUSION

In conclusion, we have studied the temperature limiting factors of QAH states by quantitatively investigating the quantum transport behavior across a range of thickness and doping of MTI as well as their magneto-optic response.

We showed that in the hybridized 2D limit (six QLs), the QAH onset temperature is mostly limited by the formation of superparamagnetic states. By introducing proper modulation doping of Cr element, we successfully enlarged the exchange gap and stabilize the ferromagnetism near zero field. However, the QAH gap size is still limited to around 1 K. We believe that the small gap size problem cannot be fully resolved by increasing the doping level alone. Because, first, magnetic doping is capped by solubility limit; second, the associated decrease in SOC when Cr substitutes the heavier element (e.g., Bi or Sb) in MTI will restrict the upper bound of magnetic doping. Beyond the doping level limit, the statistical random fluctuation of magnetic dopant is also inevitable in molecular beam epitaxy (MBE) as well as any other low-temperature epitaxy technique. This effect greatly limits the global nontrivial exchange gap size, which explains the experimental discrepancy between the local 30-meV mass gap measured by scanning tunneling microscopy (*56*, *57*) and a much smaller average activation gap size measured using transport method. On the other hand, for thicker MTI samples (8 and 10 QLs) with more robust ferromagnetism, the QAH state is affected by the bulk effect and the activation gap size is vulnerable to the vicinity of the Fermi level to the bulk valence band. As a result, the onset temperature of QAHE does not exhibit clear advantage over the 2D MTI samples.

On the basis of the results presented in this work, to further increase the QAH gap as well as its onset temperature, here, we propose two approaches. Internally, we could dope extra element that fulfills any of the following criterion: (i) element that introduces large SOC, (ii) element that promotes long-range coupling of the existing magnetic dopants, and (iii) elements that can suppress the side

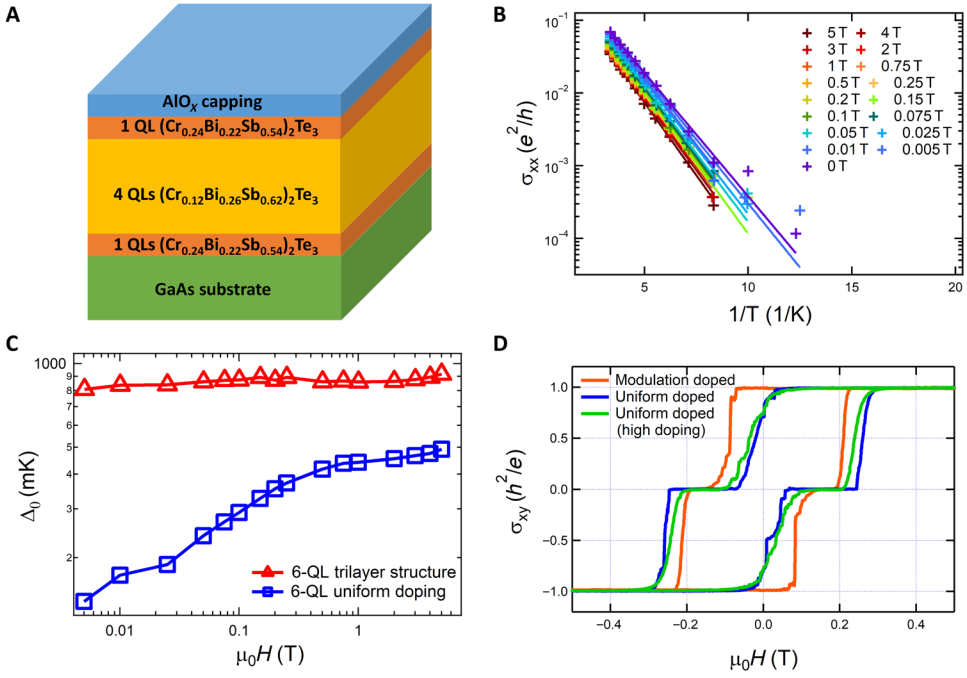

Fig. 4. Structural engineering and tunable zero-Hall plateaus in six-QL MTI samples. (**A**) Schematic drawing of the trilayer six-QL MTI structure with heavy Cr doping at top and bottom surfaces. (**B**) σ_{xx} as a function of inverse temperature for the trilayer six-QL MTI sample at different external magnetic fields. The Arrhenius fitting does not need the use of extra dissipative term. (**C**) Comparison of QAH activation energy versus external field between trilayer MTI and uniformly doped MTI. The trilayer QAH activation energy shows much less field dependency, manifesting a more robust ferromagnetism. (**D**) Hysteresis loop of σ_{xx} for the six-QL MTI samples using three different doping profiles. The widths of zero-Hall plateaus in these samples vary greatly due to the doping engineering.

valence band near the Dirac point. Externally, we could interface highly ordered FM or anti-FM insulator to counter the inhomogeneity issue and raise MTI's ordering temperature through effective exchange interactions (*58*–*60*). In addition, searching for new materials with intrinsic ferromagnetism and topological surface state has also shown promising progress especially in the $MnBi_2Te_4$ system (*61*).

Beyond the QAHE observed in current material system, we demonstrated the importance of structural engineering to functionalize QAH states, especially for the study of the chiral Majorana edge mode and axion insulators (*62*, *63*). By optimizing the thickness and doping profile of MTI, we could control the width of the zero-Hall plateaus that adds an additional dimension to manipulate the chiral Majorana edge states, which can be potentially used in fault-tolerant topological quantum computations.

MATERIALS AND METHODS

Material growth

MTI thin films were grown by the MBE method in an ultrahigh vacuum Perkin-Elmer system. Semi-insulating GaAs(111)B substrate was first cleaned ultrasonically by acetone and deionized water. After being loaded into the vacuum chamber, the substrate was first heated up to 580°C under Se-rich atmosphere to remove the native oxide. Then, the substrate was cooled down to growth temperature. During the growth, the substrate was maintained at 200°C growth temperature, with 6 N purity Bi, Sb, Te, and Cr elements co-evaporated from Knudsen cells. The epitaxial growth was in situ monitored by reflection high-energy electron diffraction (RHEED) to optimize the growth condition. After the growth, the substrate was cooled down to room temperature and 2-nm Al was evaporated from a Knudsen cell to passivate the MTI before being taken out of the ultra-high vacuum (UHV) chamber.

Transport measurement

Magneto-transport at 0.02 K < T < 0.3 K was performed in He3/He4 dilution fridge. AC bias (10 nA) was applied by sourcing 1 V RMS across a 100-megohm reference resistor at 7.351-Hz measurement frequency. The drain current, longitudinal voltage (V_{xx}), and Hall voltage (V_{yx}) were measured with SR830 lock-in amplifiers.

Optical measurement

The magneto-optic Kerr rotation experiment was done using a fiber-optic Sagnac interferometer with 10^{-8} rad DC Kerr sensitivity. The system is integrated with a dilution fridge to allow concurrent optical and transport measurement at milli-kelvin temperature range.

SUPPLEMENTARY MATERIALS

Supplementary material for this article is available at http://advances.sciencemag.org/cgi/content/full/6/25/eaaz3595/DC1

REFERENCES AND NOTES

1. K. S. Novoselov, Z. Jiang, Y. Zhang, S. V. Morozov, H. L. Stormer, U. Zeitler, J. C. Maan, G. S. Boebinger, P. Kim, A. K. Geim, Room-temperature quantum hall effect in graphene. *Science* **315**, 1379–1379 (2007).
2. F. D. M. Haldane, Model for a quantum Hall effect without Landau levels: Condensed-matter realization of the "parity anomaly". *Phys. Rev. Lett.* **61**, 2015–2018 (1988).
3. C. L. Kane, E. J. Mele, Z_2 topological order and the quantum spin Hall effect. *Phys. Rev. Lett.* **95**, 146802 (2005).
4. B. A. Bernevig, T. L. Hughes, S.-C. Zhang, Quantum spin Hall effect and topological phase transition in HgTe quantum wells. *Science* **314**, 1757–1761 (2006).

5. R. Yu, W. Zhang, H.-J. Zhang, S.-C. Zhang, X. Dai, Z. Fang, Quantized anomalous Hall effect in magnetic topological insulators. *Science* **329**, 61–64 (2010).
6. M. König, S. Wiedmann, C. Brüne, A. Roth, H. Buhmann, L. W. Molenkamp, X.-L. Qi, S.-C. Zhang, Quantum spin Hall insulator state in HgTe quantum wells. *Science* **318**, 766–770 (2007).
7. C. Z. Chang, J. S. Zhang, M. H. Liu, Z. C. Zhang, X. Feng, K. Li, L.-L. Wang, X. Chen, X. Dai, Z. Fang, X.-L. Qi, S.-C. Zhang, Y. Wang, K. He, X.-C. Ma, Q.-K. Xue, Thin films of magnetically doped topological insulator with carrier-independent long-range ferromagnetic order. *Adv. Mater.* **25**, 1065–1070 (2013).
8. C.-Z. Chang, J. S. Zhang, X. Feng, J. Shen, Z. C. Zhang, M. H. Guo, K. Li, Y. Ou, P. Wei, L.-L. Wang, Z.-Q. Ji, Y. Feng, S. Ji, X. Chen, J. Jia, X. Dai, Z. Fang, S.-C. Zhang, K. He, Y. Wang, L. Lu, X.-C. Ma, Q.-K. Xue, Experimental observation of the quantum anomalous Hall effect in a magnetic topological insulator. *Science* **340**, 167–170 (2013).
9. C.-Z. Chang, W. W. Zhao, D. Y. Kim, H. J. Zhang, B. A. Assaf, D. Heiman, S.-C. Zhang, C. Liu, M. H. W. Chan, J. S. Moodera, High-precision realization of robust quantum anomalous Hall state in a hard ferromagnetic topological insulator. *Nat. Mater.* **14**, 473–477 (2015).
10. Z. H. Zhou, Y.-J. Chien, C. Uher, Thin-film ferromagnetic semiconductors based on $Sb_{2-x}V_xTe_3$ with T_C of 177 K. *Appl. Phys. Lett.* **87**, 112503 (2005).
11. X. F. Kou, S.-T. Guo, Y. B. Fan, L. Pan, M. R. Lang, Y. Jiang, Q. Shao, T. Nie, K. Murata, J. Tang, Y. Wang, L. He, T.-K. Lee, W.-L. Lee, K. L. Wang, Scale-invariant quantum anomalous Hall effect in magnetic topological insulators beyond the two-dimensional limit. *Phys. Rev. Lett.* **113**, 137201 (2014).
12. A. J. Bestwick, E. J. Fox, X. F. Kou, L. Pan, K. L. Wang, D. Goldhaber-Gordon, Precise quantization of the anomalous Hall effect near zero magnetic field. *Phys. Rev. Lett.* **114**, 187201 (2015).
13. S. Grauer, S. Schreyeck, M. Winnerlein, K. Brunner, C. Gould, L. W. Molenkamp, Coincidence of superparamagnetism and perfect quantization in the quantum anomalous Hall state. *Phys. Rev. B* **92**, 201304 (2015).
14. M. H. Liu, W. D. Wang, A. R. Richardella, A. Kandala, J. Li, A. Yazdani, N. Samarth, N. P. Ong, Large discrete jumps observed in the transition between Chern states in a ferromagnetic topological insulator. *Sci. Adv.* **2**, e1600167 (2016).
15. J. G. Checkelsky, R. Yoshimi, A. Tsukazaki, K. S. Takahashi, Y. Kozuka, J. Falson, M. Kawasaki, Y. Tokura, Trajectory of the anomalous Hall effect towards the quantized state in a ferromagnetic topological insulator. *Nat. Phys.* **10**, 731–736 (2014).
16. Y. B. Ou, C. Liu, L. G. Zhang, Y. Feng, G. Y. Jiang, D. Y. Zhao, Y. Zang, Q. Zhang, L. Gu, Y. Wang, K. He, X. Ma, Q.-K. Xue, Heavily Cr-doped $(Bi,Sb)_2Te3$as a ferromagnetic insulator with electrically tunable conductivity. *APL Mater.* **4**, 086101 (2016).
17. E. O. Lachman, A. F. Young, A. Richardella, J. Cuppens, H. R. Naren, Y. Anahory, A. Y. Meltzer, A. Kandala, S. Kempinger, Y. Myasoedov, M. E. Huber, N. Samarth, E. Zeldov, Visualization of superparamagnetic dynamics in magnetic topological insulators. *Sci. Adv.* **1**, e1500740 (2015).
18. W. Li, M. Claassen, C.-Z. Chang, B. Moritz, T. Jia, C. Zhang, S. Rebec, J. J. Lee, M. Hashimoto, D.-H. Lu, R. G. Moore, J. S. Moodera, T. P. Devereaux, Z.-X. Shen, Origin of the low critical observing temperature of the quantum anomalous Hall effect in V-doped $(Bi, Sb)_2Te3$ film. *Sci. Rep.* **6**, 32732 (2016).
19. T. R. F. Peixoto, H. Bentmann, S. Schreyeck, M. Winnerlein, C. Seibel, H. Maaß, M. Al-Baidhani, K. Treiber, S. Schatz, S. Grauer, C. Gould, K. Brunner, A. Ernst, L. W. Molenkamp, F. Reinert, Impurity states in the magnetic topological insulator $V:(Bi,Sb)_2Te3$. *Phys. Rev. B* **94**, 195140 (2016).
20. E. O. Lachman, M. Mogi, J. Sarkar, A. Uri, K. Bagani, Y. Anahory, Y. Myasoedov, M. E. Huber, A. Tsukazaki, M. Kawasaki, Y. Tokura, E. Zeldov, Observation of superparamagnetism in coexistence with quantum anomalous Hall C = ±1 and C = 0 Chern states. *NPJ Quant. Mater.* **2**, 70 (2017).
21. X. Feng, Y. Feng, J. Wang, Y. B. Ou, Z. Q. Hao, C. Liu, Z. Zhang, L. Zhang, C. Lin, J. Liao, Y. Li, L.-L. Wang, S.-H. Ji, X. Chen, X. Ma, S.-C. Zhang, Y. Wang, K. He, Q.-K. Xue, Thickness dependence of the quantum anomalous Hall effect in magnetic topological insulator films. *Adv. Mater.* **28**, 6386–6390 (2016).
22. X. F. Kou, L. Pan, J. Wang, Y. Fan, E. S. Choi, W.-L. Lee, T. Nie, K. Murata, Q. Shao, S.-C. Zhang, K. L. Wang, Metal-to-insulator switching in quantum anomalous Hall states. *Nat. Commun.* **6**, 8474 (2015).
23. J. Wang, B. Lian, S.-C. Zhang, Universal scaling of the quantum anomalous Hall plateau transition. *Phys. Rev. B* **89**, 085106 (2014).
24. M. Mogi, M. Kawamura, R. Yoshimi, A. Tsukazaki, Y. Kozuka, N. Shirakawa, K. S. Takahashi, M. Kawasaki, Y. Tokura, A magnetic heterostructure of topological insulators as a candidate for an axion insulator. *Nat. Mater.* **16**, 516–521 (2017).
25. Y. Feng, X. Feng, Y. Ou, J. Wang, C. Liu, L.s. Zhang, D. Zhao, G. Jiang, S.-C. Zhang, K. He, X. Ma, Q.-K. Xue, Y. Wang, Observation of the zero hall plateau in a quantum anomalous Hall insulator. *Phys. Rev. Lett.* **115**, 126801 (2015).
26. J. Wang, Q. Zhou, B. Lian, S.-C. Zhang, Chiral topological superconductor and half-integer conductance plateau from quantum anomalous Hall plateau transition. *Phys. Rev. B* **92**, 064520 (2015).
27. Q. L. He, L. Pan, A. L. Stern, E. C. Burks, X. Che, G. Yin, J. Wang, B. Lian, Q. Zhou, E. S. Choi, K. Murata, X. Kou, Z. Chen, T. Nie, Q. Shao, Y. Fan, S.-C. Zhang, K. Liu, J. Xia, K. L. Wang, Chiral Majorana fermion modes in a quantum anomalous Hall insulator–superconductor structure. *Science* **357**, 294–299 (2017).
28. Y. Zhang, K. He, C.-Z. Chang, C.-L. Song, L.-L. Wang, X. Chen, J.-F. Jia, Z. Fang, X. Dai, W.-Y. Shan, S.-Q. Shen, Q. Niu, X.-L. Qi, S.-C. Zhang, X.-C. Ma, Q.-K. Xue, Crossover of the three-dimensional topological insulator Bi2Se3 to the two-dimensional limit. *Nat. Phys.* **6**, 584–588 (2010).
29. C. Liu, Y. Zang, W. Ruan, Y. Gong, K. He, X. Ma, Q.-K. Xue, Y. Wang, Dimensional crossover-induced topological hall effect in a magnetic topological insulator. *Phys. Rev. Lett.* **119**, 176809 (2017).
30. J. Linder, T. Yokoyama, A. Sudbø, Anomalous finite size effects on surface states in the topological insulator Bi_2Se_3. *Phys. Rev. B* **80**, 205401 (2009).
31. C.-X. Liu, H. Zhang, B. H. Yan, X.-L. Qi, T. Frauenheim, X. Dai, Z. Fang, S.-C. Zhang, Oscillatory crossover from two-dimensional to three-dimensional topological insulators. *Phys. Rev. B* **81**, 041307 (2010).
32. H.-Z. Lu, W.-Y. Shan, W. Yao, Q. Niu, S.-Q. Shen, Massive Dirac fermions and spin physics in an ultrathin film of topological insulator. *Phys. Rev. B* **81**, 115407 (2010).
33. M. M. Fogler, D. G. Polyakov, B. I. Shklovskii, Activated conductivity in the quantum Hall effect. *Surf. Sci.* **361–362**, 255–260 (1996).
34. A. J. M. Giesbers, U. Zeitler, M. I. Katsnelson, L. A. Ponomarenko, T. M. Mohiuddin, J. C. Maan, Quantum-Hall activation gaps in graphene. *Phys. Rev. Lett.* **99**, 206803 (2007).
35. G. S. Boebinger, H. L. Stormer, D. C. Tsui, A. M. Chang, J. C. M. Hwang, A. Y. Cho, C. W. Tu, G. Weimann, Activation energies and localization in the fractional quantum Hall effect. *Phys.Rev. B* **36**, 7919–7929 (1987).
36. R. Yoshimi, K. Yasuda, A. Tsukazaki, K. S. Takahashi, N. Nagaosa, M. Kawasaki, Y. Tokura, Quantum Hall states stabilized in semi-magnetic bilayers of topological insulators. *Nat. Commun.* **6**, 8530 (2015).
37. G. S. Boebinger, A. M. Chang, H. L. Stormer, D. C. Tsui, Magnetic field dependence of activation energies in the fractional quantum Hall effect. *Phys. Rev. Lett.* **55**, 1606–1609 (1985).
38. K. I. Bolotin, F. Ghahari, M. D. Shulman, H. L. Stormer, P. Kim, Observation of the fractional quantum Hall effect in graphene. *Nature* **462**, 196–199 (2009).
39. A. Tsukazaki, S. Akasaka, K. Nakahara, Y. Ohno, H. Ohno, D. Maryenko, A. Ohtomo, M. Kawasaki, Observation of the fractional quantum Hall effect in an oxide. *Nat. Mater.* **9**, 889–893 (2010).
40. C. Michel, P. J. Klar, S. D. Baranovskii, P. Thomas, Influence of magnetic-field-induced tuning of disorder and band structure on the magnetoresistance of paramagnetic dilute magnetic semiconductors. *Phys. Rev. B* **69**, 165211 (2004).
41. H.-B. Wu, K. Chang, J.-B. Xia, Electronic structure of diluted magnetic semiconductor superlattices: In-plane magnetic field effect. *Phys. Rev. B* **65**, 195204 (2002).
42. J.-M. Zhang, W. M. Ming, Z. G. Huang, G.-B. Liu, X. F. Kou, Y. Fan, K. L. Wang, Y. Yao, Stability, electronic, and magnetic properties of the magnetically doped topological insulators Bi_2Se_3, Bi_2Te_3, and Sb_2Te_3. *Phys. Rev. B* **88**, 235131 (2013).
43. J. Xia, Y. Maeno, P. T. Beyersdorf, M. M. Fejer, A. Kapitulnik, High resolution polar Kerr effect measurements of Sr_2RuO_4: Evidence for broken time-reversal symmetry in the superconducting state. *Phys. Rev. Lett.* **97**, 167002 (2006).
44. C.-Y. Yang, S.-J. Chang, M.-H. Lee, K.-H. Shen, S.-Y. Yang, H.-J. Lin, Y.-C. Tseng, Competing anisotropy-tunneling correlation of the CoFeB/MgO perpendicular magnetic tunnel junction: An electronic approach. *Sci. Rep.* **5**, 17169 (2015).
45. C.-M. Liu, Y.-C. Tseng, C. Chen, M.-C. Hsu, T.-Y. Chao, Y.-T. Cheng, Superparamagnetic and ferromagnetic Ni nanorod arrays fabricated on Si substrates using electroless deposition. *Nanotechnology* **20**, 415703 (2009).
46. A. Aharoni, *Introduction to the Theory of Ferromagnetism* (Oxford Univ. Press, ed. 2, 2000).
47. B. D. Cullity, C. D. Graham, *Introduction to Magnetic Materials* (IEEE/Wiley, ed. 2, 2009).
48. Y.-J. Ke, X.-Q. Zhang, Y. Ma, Z.-H. Cheng, Anisotropic magnetic entropy change in $RFeO_3$ single crystals (R = Tb, Tm, or Y). *Sci. Rep.* **6**, 19775 (2016).
49. S. Cao, H. Zhao, B. Kang, J. Zhang, W. Ren, Temperature induced spin switching in $SmFeO_3$ single crystal. *Sci. Rep.* **4**, 5960 (2015).
50. L. B. Duffy, A. I. Figueroa, Ł. Gładczuk, N.-J. Steinke, K. Kummer, G. van der Laan, T. Hesjedal, Magnetic proximity coupling to Cr-doped Sb_2Te_3 thin films. *Phys. Rev. B* **95**, 224422 (2017).
51. M. Ye, W. Li, S. Zhu, Y. Takeda, Y. Saitoh, J. Wang, H. Pan, M. Nurmamat, K. Sumida, F. Ji, Z. Liu, H. Yang, Z. Liu, D. Shen, A. Kimura, S. Qiao, X. Xie, Carrier-mediated ferromagnetism in the magnetic topological insulator Cr-doped $(Sb,Bi)_2Te_3$. *Nat. Commun.* **6**, 8913 (2015).
52. S. K. Kushwaha, I. Pletikosić, T. Liang, A. Gyenis, S. H. Lapidus, Y. Tian, H. Zhao, K. S. Burch, J. Lin, W. Wang, H. Ji, A. V. Fedorov, A. Yazdani, N. P. Ong, T. Valla, R. J. Cava, Sn-doped Bi1.1Sb0.9Te2S bulk crystal topological insulator with excellent properties. *Nat. Commun.* **7**, 11456 (2016).
53. Y. Xu, I. Miotkowski, C. Liu, J. F. Tian, H. Nam, N. Alidoust, J. Hu, C.-K. Shih, M. Z. Hasan, Y. P. Chen, Observation of topological surface state quantum Hall effect in an intrinsic three-dimensional topological insulator. *Nat. Phys.* **10**, 956–963 (2014).

54. M. Mogi, R. Yoshimi, A. Tsukazaki, K. Yasuda, Y. Kozuka, K. S. Takahashi, M. Kawasaki, Y. Tokura, Magnetic modulation doping in topological insulators toward higher-temperature quantum anomalous Hall effect. *Appl. Phys. Lett.* **107**, 182401 (2015).
55. Z. Yue, M. E. Raikh, Smearing of the quantum anomalous Hall effect due to statistical fluctuations of magnetic dopants. *Phys. Rev. B* **94**, 155313 (2016).
56. I. Lee, C. K. Kim, J. Lee, S. J. L. Billinge, R. D. Zhong, J. A. Schneeloch, T. Liu, T. Valla, J. M. Tranquada, G. Gu, J. C. S. Davis, Imaging Dirac-mass disorder from magnetic dopant atoms in the ferromagnetic topological insulator $Cr_x(Bi_{0.1}Sb_{0.9})_{2-x}Te_3$. *Proc. Natl. Acad. Sci. U.S.A.* **112**, 1316–1321 (2015).
57. C.-C. Chen, M. L. Teague, L. He, X. Kou, M. Lang, W. Fan, N. Woodward, K.-L. Wang, N.-C. Yeh, Magnetism-induced massive Dirac spectra and topological defects in the surface state of Cr-doped Bi_2Se_3-bilayer topological insulators. *New J. Phys.* **17**, 113042 (2015).
58. C. Tang, C.-Z. Chang, G. Zhao, Y. Liu, Z. Jiang, C.-X. Liu, M. R. McCartney, D. J. Smith, T. Chen, J. S. Moodera, J. Shi, Above 400-K robust perpendicular ferromagnetic phase in a topological insulator. *Sci. Adv.* **3**, e1700307 (2017).
59. X. Che, K. Murata, L. Pan, Q. L. He, G. Yu, Q. Shao, G. Yin, P. Deng, Y. Fan, B. Ma, X. Liang, B. Zhang, X. Han, L. Bi, Q.-H. Yang, H. Zhang, K. L. Wang, Proximity-induced magnetic order in a transferred topological insulator thin film on a magnetic insulator. *ACS Nano* **12**, 5042–5050 (2018).
60. M. Mogi, T. Nakajima, V. Ukleev, A. Tsukazaki, R. Yoshimi, M. Kawamura, K. S. Takahashi, T. Hanashima, K. Kakurai, T.-h. Arima, M. Kawasaki, Y. Tokura, Large anomalous Hall effect in topological insulators with proximitized ferromagnetic insulators. *Phys. Rev. Lett.* **123**, 016804 (2019).
61. Y. Deng, Y. Yu, M. Z. Shi, Z. Guo, Z. Xu, J. Wang, X. H. Chen, Y. Zhang, Quantum anomalous Hall effect in intrinsic magnetic topological insulator $MnBi_2Te_4$. *Science* **367**, 895–900 (2020).
62. D. Xiao, J. Jiang, J.-H. Shin, W. Wang, F. Wang, Y.-F. Zhao, C. Liu, W. Wu, M. H. W. Chan, N. Samarth, C.-Z. Chang, Realization of the axion insulator state in quantum anomalous Hall sandwich heterostructures. *Phys. Rev. Lett.* **120**, 056801 (2018).
63. M. Mogi, M. Kawamura, A. Tsukazaki, R. Yoshimi, K. S. Takahashi, M. Kawasaki, Y. Tokura, Tailoring tricolor structure of magnetic topological insulator for robust axion insulator. *Sci. Adv.* **3**, eaao1669 (2017).

Acknowledgments: We thank D. Goldhaber-Gordon for valuable discussions. **Funding:** This work is supported as part of the Spins and Heat in Nanoscale Electronic Systems (SHINES), an Energy Frontier Research Center funded by the U.S. Department of Energy (DOE), Office of Science, Basic Energy Sciences (BES), under award no. DE-SC0012670. We also acknowledge the support from the Army Research Office Multidisciplinary University Research Initiative (MURI) program accomplished under grant numbers W911NF-16-1-0472 and W911NF-15-1-10561. X.K. acknowledges the support from the National Key R&D Program of China under contract number 2017YFA0305400, the National Natural Science Foundation of China (grant no. 61874172), the Strategic Priority Research Program of Chinese Academy of Sciences (grant no. XDA18010000), and the Shanghai Sailing program under contract number 17YF1429200. Q.L.H. acknowledges the support from the National Natural Science Foundation of China (grant no. 11874070), the National Key R&D Program of China (grant no. 2018YFA0305601), the Strategic Priority Research Program of Chinese Academy of Sciences (grant no. XDB28000000), and National Thousand-Young Talents Program in China. The work at UC Irvine was supported by NSF grant DMR-1807817. A portion of this work was performed at the National High Magnetic Field Laboratory, which is supported by National Science Foundation Cooperative agreement nos. DMR-1157490 and DMR-1644779 and the State of Florida. **Author contributions:** L.P., X.K., and K.L.W. designed the experiment. L.P., Q.L.H., and P.Z. grew the samples. X.C. fabricated the samples. L.P., Q.L.H., A.S., B.C., E.S.C., J.X., and X.K. performed the measurements. L.P., X.L., Q.L.H., G.Y., P.D., Q.S., C.-Y.Y., and X.K. carried out the analysis and modeling of the results. L.P., X.K., and K.L.W. wrote the manuscript with input from all authors. **Competing interests:** The authors declare that they have no competing interests. **Data and materials availability:** All data needed to evaluate the conclusions in the paper are present in the paper and/or the Supplementary Materials. Additional data related to this paper may be requested from the authors.

Submitted 4 September 2019
Accepted 5 May 2020
Published 17 June 2020
10.1126/sciadv.aaz3595

Citation: L. Pan, X. Liu, Q. L. He, A. Stern, G. Yin, X. Che, Q. Shao, P. Zhang, P. Deng, C.-Y. Yang, B. Casas, E. S. Choi, J. Xia, X. Kou, K. L. Wang, Probing the low-temperature limit of the quantum anomalous Hall effect. *Sci. Adv.* **6**, eaaz3595 (2020).

Probing the low-temperature limit of the quantum anomalous Hall effect

Lei Pan, Xiaoyang Liu, Qing Lin He, Alexander Stern, Gen Yin, Xiaoyu Che, Qiming Shao, Peng Zhang, Peng Deng, Chao-Yao Yang, Brian Casas, Eun Sang Choi, Jing Xia, Xufeng Kou and Kang L. Wang

Sci Adv **6** (25), eaaz3595.
DOI: 10.1126/sciadv.aaz3595